Experimental study of the effect of a slat on the aerodynamic performance of a thick base airfoil

Axelle Viré[1], Bruce LeBlanc[1], Julia Steiner[1], and Nando Timmer[1]

[1]Wind Energy Section, Faculty of Aerospace Engineering, Delft University of Technology, Delft, The Netherlands

Correspondence: Axelle Viré (a.c.vire@tudelft.nl)

Abstract.

There is continuous effort to try and improve the aerodynamic performance of wind turbine blades. This experimental study focusses on the addition of a passive slat on a thick airfoil typically used in the inboard part of commercial wind turbine blades. Nine different slat configurations are considered, with both a clean and tripped main airfoil. The results are compared with the performances of the airfoil without slat, as well as the airfoil equipped with vortex generators. It is found that, when the airfoil is clean, the increase in lift-to-drag ratio due to the presence of a slat is larger than when vortex generators are used. This is also true for the tripped airfoil, but only at small angles of attack. As expected, in all configurations, the presence of the slat delays flow separation and stall. Finally, for a clean airfoil and small angles of attack, the slat decreases the lift-to-drag ratio of the main airfoil only. By contrast, as the angle of attack increases, it seems that the slat changes the flow field around the main airfoil in such a way that its lift-to-drag ratio becomes larger than for the airfoil without slat. These effects are less pronounced when the airfoil is tripped. This work helps to better understand the role of a slat in improving the aerodynamics of blade sections. It can also be used to validate simulation tools in the field.

1 Introduction

The development of innovative add-ons, and their combination, are topics of high interest for wind turbine manufacturers. Such devices can increase the energy yield of a wind turbine by a few percent, leading to potentially significant reductions in levelised cost of energy. Add-on devices are already commonly used on commercial wind turbine blades. The type of add-ons, and their location along the blade, depend on the target objective which is often to improve the aerodynamic performances of the rotor. A good example of such devices are low-drag vortex generators (VGs), which are typically used at the inboard or mid-board sections of the blade. At these locations, the airfoil sections are rather thick with a high maximum lift in order to allow for the chord length to be reduced, without penalising greatly the overall energy yield. Thick airfoils inboard are also useful to reduce standstill loads under extreme conditions. However, the inboard part of the blade typically operates under large angles of attack. Hence, large flow separation may occur at these locations. In order to mitigate this, and increase the lift-to-drag ratio, vortex generators can be positioned in arrays in front of the separation line. These devices trigger the formation of small vortices in the boundary layer that re-energise the near-wall flow, hence preventing the flow to separate (Schubauer and Spangenberg, 1960). VGs are one type of wind turbine add-ons. Other types of devices are commonly used as well, either

to increase aerodynamic performance or to reduce trailing edge noise. Furthermore, add-ons can be either active or passive, depending on whether their characteristics change in time.

This work focusses on passive flow control devices that increase aerodynamic performance. In this context, aside from VGs, inboard devices include Gurney flaps, which increase the lift force on the blade section by increasing the effective camber
30 when placed on the pressure side and close to the trailing edge (Liebeck, 1978; Bach, 2016). Spoilers are another option and enhance the contribution of the lift and torque (Wentz, 1975). By contrast, add-ons can also be used outboard. This is the case of winglets, which are placed at the blade tip to reduce the downwash of the tip vortex, and therefore, decrease drag (Velte et al., 2016). A combination of multiple flow control devices can also be used on a given blade. An overview of this is given, for example, by Baldacchino (2019).

35 Although slats have been widely used in the aircraft industry, they are currently not used on commercial wind turbine blades. They could however be beneficial in the inboard part of the blade in order to delay the onset of stall, which is susceptible to occur due to the large angles of attack at these locations.The effect of a leading-edge slat on the flow field is however complex (Smith, 1975). Therefore, careful slat design and positioning are needed to ensure that the static stall angle of the main airfoil is increased, without overly increasing drag or causing a mixing between the wake of the slat and the boundary layer on the
40 main airfoil (Smith, 1975). In the last decade, the potential benefits of slats have also been investigated on thick airfoils. In this context, experimental studies report that the presence of a slat delays stall and increases the maximum lift coefficient (Pechli-vanoglou et al., 2010; Zahle et al., 2012). Interestingly, Zahle et al. (2012) further compared results from computational fluid dynamics (CFD) and experiments with an overall good agreement. However, the experimental measurements were polluted by three-dimensional wall effects at large angles of attack. Additionally, Manso Jaume and Wild (2016) looked at a numeri-
45 cal shape optimisation of both the slat and the main airfoil profile. The study showed that a combined optimisation leads to better aerodynamic performance than the superposition of both profiles optimised individually. Finally, Steiner et al. (2020) performed a parametric analysis using CFD simulations to optimise the design of a slat in combination with a thick airfoil at a Reynolds number of $Re = 10^7$. It was shown that a slat with a chord length equal to 30% of that of the main airfoil offers the aerodynamic benefit of a slat with a 40% chord length, without leading to a high positive pitching moment. Also, the increase
50 in stall angle and maximum glide ratio, due to the presence of the slat, was higher when the thickness of the main profile was increased.

The purpose of the present work is to explore experimentally the effectiveness of using a leading-edge slat on a thick base airfoil commonly used in commercial wind turbine blades. It also complements the numerical results obtained by Steiner et al. (2020) on a very similar setup. The paper is organised as follows. Section 2 describes the experimental setup, data acquisition,
55 and post-processing methodology. Section 3 shows the results of the wind tunnel tests with a thick main airfoil and a variety of configurations, namely: (i) without add-ons, (ii) with a leading-edge slat ~~at two Reynolds numbers and~~ with a range of slat parameters, and (iii) with vortex generators. Finally, Section 4 summarises the main conclusions of this study.

2 Methodology

2.1 Experimental setup

The experiment is conducted in the low-speed low-turbulence tunnel (LTT) of Delft University of Technology[1]. This is an atmospheric wind tunnel of the closed-throat single-return type, with interchangeable octagonal test sections with a length of 2.6 metres, a width of 1.80 metres and a height of 1.25 metres. The maximum Reynolds number for two-dimensional testing is about 3.5 million. Here, the experiments are conducted at a Reynolds numbers of $Re = 1.5 \cdot 10^6$. The experimental setup consists of the following components: the main airfoil model, the slat, and the attachment mechanism for testing different slat configurations.

The main element is a composite DU00-W2-401 airfoil model with a chord length of $c_{\mathrm{main}} = 0.5m$. The model was mounted vertically in the test section on two aluminium attachment plates flush with rotating discs in the upper and lower tunnel wall that provide changes in angle of attack. The slat profile is a custom, cambered airfoil with a chord length equal to $0.3c_{\mathrm{main}}$, as this was shown to lead to good performances in Steiner et al. (2020). The coordinates of the slat element are available in LeBlanc et al. (2021). The slat is 3D-printed with an internal structure consisting of stiffening ribs and a hexagonal steel rod, providing attachment to the aluminium plate and taking up the loads on the slat at high wind speeds (see Fig. 2, left). The slat surface is smoothed with sandpaper and finished with spray paint. In this study, the streamwise position of the slat trailing-edge is fixed at $s_{\mathrm{slat}} = 0.151c_{\mathrm{main}}$. The effect of two parameters are investigated, as shown in Fig.1: (i) the gap width h_{slat} between the main airfoil and the slat trailing edge, and (ii) the slat angle β_{slat} relative to the main airfoil. In order to vary these parameters, the steel rod has pre-manufactured set points in the mounting plate corresponding to pre-determined values of h_{slat} and β_{slat}. Figure 2 shows CAD views of the cross-section of the slat (left) and the end plate (right). The set of configurations investigated here, and their associated labels, is presented in Table 1. The values of the slat angle β_{slat} are chosen based on previous works (Steiner et al., 2020; Schramm et al., 2016; Manso Jaume and Wild, 2016), which show that a slat angle of around $20°$ leads to the best performance. In order to assess the sensitivity of the results to β_{slat}, three different values separated by $5°$ are considered here, namely $\beta_{\mathrm{slat}} = 16.4°, 21.4°, 26.4°$. It is also expected that reducing the gap width h_{slat}, while avoiding confluent boundary layers, increases the positive effect brought by the slat. However, the results obtained by Steiner et al. (2020) with a 2% gap width (i.e. $h_{\mathrm{slat}}/c_{\mathrm{main}} = 0.02$) led to smaller lift coefficients, smaller lift-over-drag ratios, and a similar stall angle than with a 4% gap width. In this study, three values of the gap width varying between 2% and 4% are therefore investigated.

---

[1]https://www.tudelft.nl/en/ae/organisation/departments/aerodynamics-wind-energy-flight-performance-and-propulsion/facilities/low-speed-wind-tunnels/low-turbulence-tunnel/
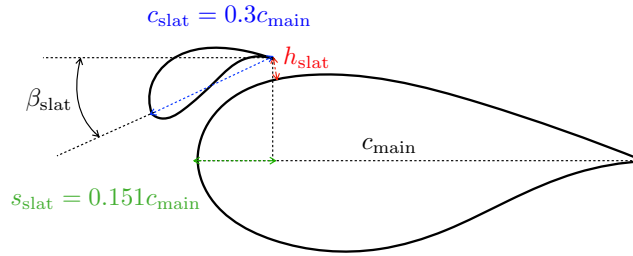
Figure 1. Illustration of the slat parameters of interest in this work: gap width h_{slat} between the main airfoil and the slat, and (ii) the slat angle β_{slat} relative to the main airfoil.
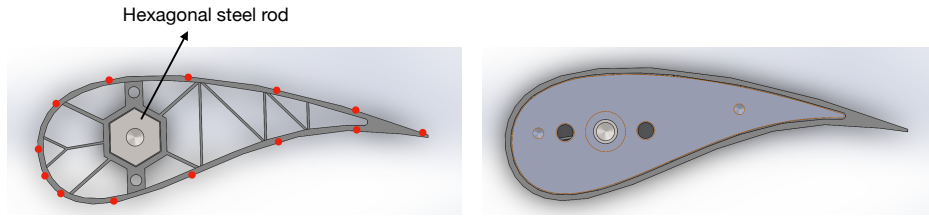
Figure 2. CAD design of the slat cross-section (left) and end plate (right). Red dots on the left figure indicate the location of the pressure tabs.

Table 1. Set of configurations and associated labels.

Configuration ~~name~~ labels	~~h_{slat}/c_{main}~~ $h_{slat}/c_{main} = 0.02$	~~β_{slat}°~~ $h_{slat}/c_{main} = 0.03$	$h_{slat}/c_{main} = 0.0$
$\beta_{slat} = 16.4°$	A	~~0.02~~ D	~~16.4~~ G
$\beta_{slat} = 21.4°$	B	~~0.02~~ E	~~21.4~~ H
$\beta_{slat} = 26.4°$	C	~~0.02 26.4 D 0.03 16.4 E 0.03 21.4~~ F	~~0.03 26.4~~ I
~~G 0.04 16.4 H 0.04 21.4 I 0.04 26.4~~ height			

In order to mitigate interference effects due to the tunnel wall boundary layers, pairs of vortex generators (VGs) are installed on the main profile close to the walls, on both the pressure and suction sides of the main airfoil, as shown by Fig. 3 (showing the suction side only). The geometrical characteristics of these VGs, as defined in Fig. 4, are as follows: $h/c_{main} = 0.01$, $l/h = 3.4$, $z/h = 7$, $s/h = 2$, and $\beta = 16.4°$. As it will be shown in Section 3, this helps reducing three-dimensional flow effects on the measured pressure distributions. Since vortex generators are commonly used to improve the performances of wind turbine blades, this paper also presents results obtained when placing VGs on the main airfoil alone. In that case, the VGs are placed at $x/c_{main} = 0.35$. ~~The geometrical characteristics of the VGs are shown in Fig. 4 and the parameter values are~~, which is a good compromise between increasing lift coefficient and reducing the associated drag penalty. The parameter values of these VGs are as follows: $h/c_{main} = 0.01$, $l/h = 2.2$, $z/h = 7.6$, $s/h = 3.2$, and $\beta = 15.8°$. The results obtained with the VGs alone are compared with the performances obtained with a slat.
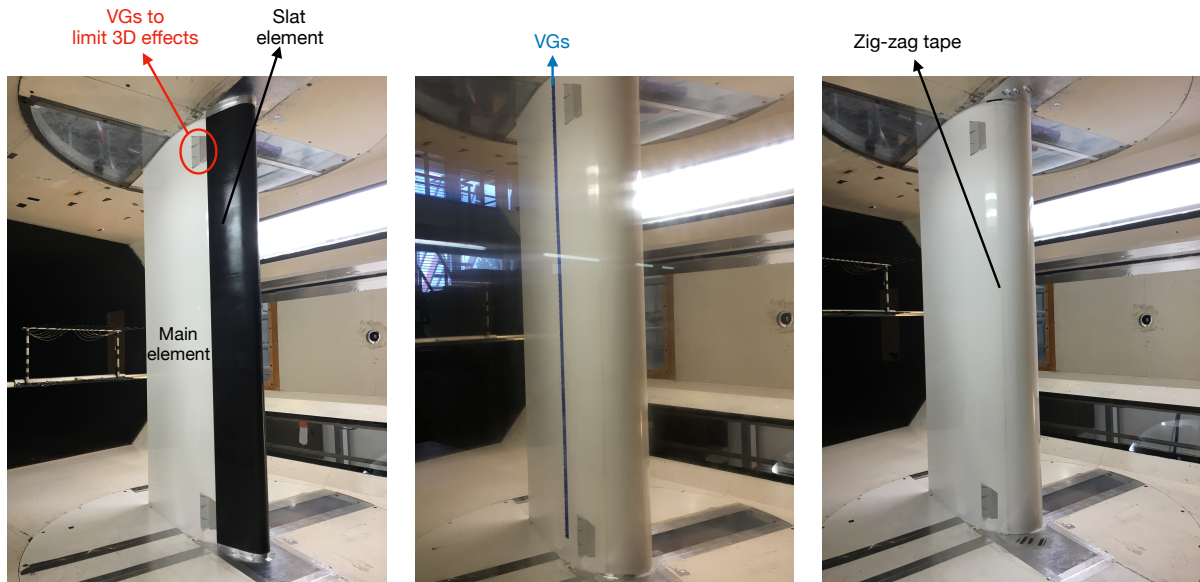
Figure 3. Photographs of the experimental setup: main profile with slat element (left), main profile with vortex generators (centre), main profile with zig-zag tape (right). In all the cases, VGs are used close to the walls to limit three-dimensional effects. This is highlighted in red on the left picture.
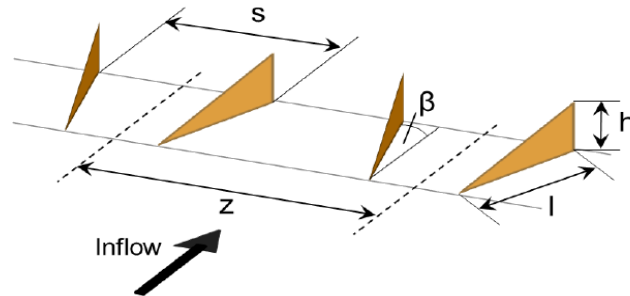
Figure 4. Illustration of the geometrical characteristics of the vortex generators.

Finally, all the tests are performed with both a clean and a tripped main airfoil. For the tripped cases, a zig-zag turbulator

95 is placed on the main airfoil, as shown on the right photograph in Fig. 3. The details about the setup are given in Section 3.2. Note that an analysis on different tripping methods has not been performed and could be useful for future studies.

2.2 Data acquisition and post-processing

The lift and drag coefficients on the airfoil and slat can be determined by using a combination of pressure measurements on the airfoil surfaces and using a wake rake. On the airfoil surfaces, the normal force coefficient C_n' is obtained by integrating

the pressure distribution from 94 and ~~11~~ 13 pressure orifices in the main element and the slat, respectively. ~~For small angles, the measured lift coefficient C_l' is expressed as~~

, that is

$$C_{l_n}' = \frac{C_n'}{\cos(\alpha)} - \int_0^1 \left(C_d' \tan(\alpha)_{p,l} - C_{p,u} \right) d\left(\frac{x}{c} \right),$$
(1)

where C_d' is the uncorrected drag coefficient measured with the wake rake and α is the angle of attack. ~~The measured lift, drag and moments coefficients are corrected for lift interference, solid and wake blockage, and wake buoyancy according to the correction equation given by AGARDograph 336 (AGARD-AG-336, 1998), while the pressure distributions are corrected according to the method of Allen and Vincenti (1944), i. e.~~

$$C_l = C_l' \left(1 - t_1 - t_2 + t_3 - t_4 \right),$$

~~where~~

$$t_1 = \frac{\sigma}{\beta^2},$$

$$t_2 = 5.25 \frac{\sigma^2}{\beta^4},$$

$$t_3 = \frac{2 - M^2}{\beta^3} \Lambda \sigma \left(1 + \frac{1.1\beta c}{t} \right) \alpha^2,$$

$$t_4 = \frac{(2 - M^2)(1 + 0.4M^2)}{(4\beta^2)} \frac{c}{h} C_d',$$

$C_{p,l}$ and ~~$\sigma = \pi^2/48(c/h)^2$ is~~ $C_{p,u}$ are the pressure coefficients on the lower and upper surface, respectively, and c is the chord of the element being considered (either main element or slat). Note that primed coefficients denote uncorrected values. Also, the ~~wind tunnel blockage factor, $\beta = \sqrt{1 - M^2}$ is the compressibility factor, M is the measured apparent upstream Mach number, and the body shape factor is set to $\Lambda = 0.9087$. Primed coefficients denote uncorrected values. Pre-stall, drag~~ low number of pressure tabs on the slat leads to an integration error of about 11%. This is quantified by comparing the integration of C_p distributions obtained from Xfoil using, on the one hand, all the slat coordinates and, on the other hand, only the data at the locations of the pressure tabs. The drag coefficient pre-stall is measured using a wake rake placed behind the airfoil. The wake rake has 67 total pressure tubes and 16 static pressure tubes. The uncorrected drag coefficient C_d' measured with the wake rake is given by

$$C_d' = \frac{2}{c} \int_{wake} \sqrt{C_{p,t} - C_{p,s}} \left(1 - \sqrt{C_{p,t}} \right) dy,$$
(2)

where $C_{p,t}$ and $C_{p,s}$ are the total and static pressure in the wake, respectively. When the wake becomes unstable or wider than the wake rake, the latter cannot be used to measure drag. Therefore, post-stall, the pressure ~~lift and drag are used~~ measurements on the airfoil and slat surfaces are used instead. The angle of attack at which the switch is made between wake-rake drag and

pressure drag is determined based on identifying flow separation from the measurements. These angles also correspond to C_l values that are slightly smaller than the maximum for a given case. The exact values are reported in AppendixA. For small angles, the measured lift coefficient C_l' is expressed as

$$C_l' = \frac{C_n'}{\cos(\alpha)} - C_d' \tan(\alpha), \tag{3}$$

where α is the angle of attack. The measured lift, drag, and angle of attack are corrected following the methods described in Allen and Vincenti (1944); AGARD-AG-109 (1966), i.e.

$$C_l = C_l'(1 - t_1 - t_2 + t_3 - t_4), \tag{4}$$

where

$$t_1 = \frac{\sigma}{\beta^2}, \tag{5}$$

$$t_2 = 5.25 \frac{\sigma^2}{\beta^4}, \tag{6}$$

$$t_3 = \frac{2 - M^2}{\beta^3} \Lambda \sigma \left(1 + \frac{1.1\beta c}{t}\right) \alpha^2, \tag{7}$$

$$t_4 = \frac{(2 - M^2)(1 + 0.4M^2)}{(4\beta^2)} \frac{c}{h} C_d', \tag{8}$$

and $\sigma = \pi^2/48(c/h)^2$ is the wind tunnel blockage factor, $\beta = \sqrt{1 - M^2}$ is the compressibility factor, M is the measured apparent upstream Mach number, c is the element chord length, h is the wind tunnel height, t is the airfoil thickness, and the body shape factor is set to $\Lambda = 0.9087$. ~~The angle of attack at which the switch is made between wake-rake drag and pressure drag is deter~~ Independently of whether wake-rake or pressure drag is used, the resulting measured drag coefficient C_d' is corrected as

$$C_d = C_d'(1 - \Delta C_d - t_3 - t_4), \tag{9}$$

where the wake buoyancy correction is $\Delta C_d = 0$ when using the wake rake, and otherwise,

$$\Delta C_d = \Lambda \sigma \frac{1 + 0.4M^2}{\beta^3} \left(1 + \frac{1.1\beta c}{t} \alpha^2\right). \tag{10}$$

It must be noted that the present corrections are only valid until about an angle of attack of $20°$. In situations where significant separation plays a role, these equations underestimate the effect of wake blockage and consequently may give too optimistic lift coefficients. As this is mainly a comparative study, no effort has been undertaken to account for the additional blockage due to separation. Also, all the results are shown up to an angle of attack of $20°$.

Data are recorded using an electronic data acquisition system and are on line reduced to show corrected force and moment coefficients and pressure distributions. A thermal camera enables to visualise the location of flow transition along with the pressure distribution. Wool tufts are also placed on the base airfoil to have a measure of flow separation and identify possible three-dimensional wall effects during testing.

3 Results

3.1 Sensitivity to slat position

Figure 5 shows the lift coefficient C_l as a function of the angle of attack α for different slat configurations, a clean main airfoil (i.e. no tripping), and at a Reynolds number of $Re = 1.5 \cdot 10^6$. The black dots represent the lift coefficient in the absence of a slat. In ~~that case, the~~ order to verify the experimental setup, the results of Xfoil simulations are also shown (continuous black line). There is a good agreement between Xfoil and experimental results in the linear part of the polar curve. The experimental results show that the maximum lift coefficient on the main airfoil is reached at around $\alpha = 10°$ and remains close to unity as the angle of attack is further increased. At $\alpha \approx 13°$, the lift coefficient presents a slight increase which is not expected. This feature did consistently appear for multiple repetitions of the test, even after cleaning the main profile. Therefore, a possible reason for this small disparity could be related to three-dimensional wall effects. Additionally, running the test at a slightly higher Reynolds number ($Re = 2 \cdot 10^6$) made this feature disappear. For $\alpha > 20°$, the main airfoil enters deep stall and the experimental results ~~should be~~ are disregarded. When a slat is added, the disparity around $\alpha \approx 13°$ also disappears~~and tuft visualisations.~~ Tuft visualisations, such as the one presented in Fig. 6, were performed up to $\alpha = 11°$ and demonstrate that the flow is rather two-dimensional as expected~~(Fig. 6).~~. The total maximum lift coefficient is significantly increased (factor up to 2.5) in comparison to the case without slat. For a given gap between the slat and the airfoil, the lift coefficient also increases as the slat angle β_{slat} decreases~~, except for the~~. This is valid across the set of parameters investigated here. Note that with the smallest gap and angle investigated, i.e. $h_{\text{slat}}/c_{main} = 0.02$ and $\beta_{\text{slat}} = 16.4°$ ~~, which~~ (Config A), the flow stalls already at around $\alpha \approx 15°$~~.~~ ~~The fact that stall is delayed at increasingly large slat angle is expected due to the increase of effective cambering as β_{slat} increases~~, which is smaller than in the other cases. Changing the slat gap width, for a given slat angle, does not significantly change the lift coefficient at a given angle of attack. Similarly to Fig. 5, Fig. 7 shows the drag coefficient C_d as a function of the angle of attack. ~~It is apparent that, for all the slat configurations, the total drag coefficient in the range $0° \leq \alpha \leq 7°$ is unaffected by the presence of the slat. For larger~~ At all angles of attack, the drag coefficient ~~is reduced due to the presence~~ with slat is larger than that without slat, which is expected as the slat introduces additional friction losses. The benefit of the slat ~~.~~ ~~This observation might be affected by the accuracy of the drag measurements, especially when the wake rake is used. However, these tren~~ ~~For completeness,~~ on the overall aerodynamics is highlighted in Fig. 8 that shows the ratio of lift-to-drag coefficients as a function of α. Two types of symbols are used: dots represent the data for the ensemble airfoil+slat, whilst crosses are the lift-to-drag values integrated on the main airfoil only. It is clear that, for all the configurations considered here, the overall aerodynamic performances of the ensemble airfoil+slat are improved in the presence of the slat, at least when $\alpha \geq 3°$. It is interesting to note that, for $\alpha \approx 8°$, the lift-to-drag ratio computed on the main airfoil only (coloured crosses) is smaller than the lift-to-drag ratio of the airfoil without slat (black dots). Thus, at small angles of attack, the increase in aerodynamic performance for the slat configurations is largely due to the slat itself. In particular, the presence of a slat decreases the lift force on the main airfoil, whilst it has a negligible effect on the drag force (not shown). This is in agreement with the description of Smith (1975). By contrast, at angles of attack larger than $8°$, the lift-to-drag ratio on the main airfoil alone (coloured crosses) is larger than that on the airfoil without slat (black dots). This means that the slat changes the flow field around the main airfoil in such a way that the aerodynamic per-
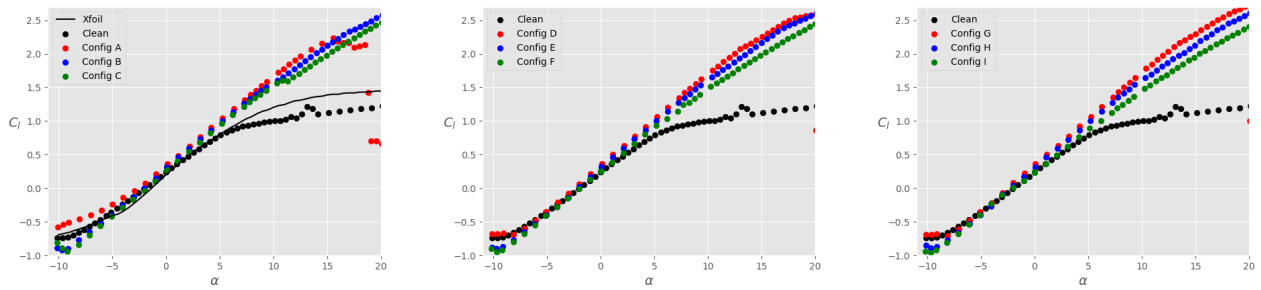
Figure 5. Total lift coefficient C_l on the ensemble airfoil+slat as a function of the angle of attack α, for different slat configurations, a clean main airfoil (i.e. no tripping), and $Re = 1.5 \cdot 10^6$: $h_{\text{slat}}/c_{main} = 0.02$ (left), $h_{\text{slat}}/c_{main} = 0.03$ (center), $h_{\text{slat}}/c_{main} = 0.04$ (right). The black data are taken without slat, while the coloured data is in the presence of a slat with $\beta_{\text{slat}} = 16.4°$ (red), $\beta_{\text{slat}} = 21.4°$ (blue), $\beta_{\text{slat}} = 26.4°$ (green). The results of Xfoil simulations for the clean main airfoil are shown by the continuous black line on the left plot.

formance of the main airfoil itself is increased. As expected, this increase is further amplified when the contribution of the lift force on the slat is added (coloured dots). Again, the slat has a negligible effect on the drag force experienced by the main airfoil

190   ~~and the lift-to-drag ratios are consistent with those obtained by CFD simulations in similar conditions Steiner et al. (2020).~~ and the lift-to-c

~~Tuft visualisation for a clean airfoil with a slat.~~

Figure 9 shows the pressure distributions of the clean airfoil (left) and the airfoil with slat in case A (right) at an angle of attack $\alpha = 10°$. It is clear that the pressure distribution on the main airfoil suction surface is significantly impacted by the

195   presence of the slat. Due to the ~~higher pressure~~ circulation on the slat ~~lower surface~~ element, the low-pressure peak on the main airfoil is reduced, also reducing the adverse pressure gradient towards the trailing edge. This enables the flow to stay attached up to the trailing edge, while the model without slat shows separation right from the mid-chord location.

This is mimicked by the associated infrared images presented in Fig. 10, with flow coming from the right. The model without slat (left) shows a small laminar separation bubble followed by transition indicated by the thin dark band at about

200   one-third of the chord. Separation may be hard to see in this picture. It is indicated by the lightest grey area. Both transition and separation locations may have been slightly influenced by the presence of the pressure orifices located in the lower part of the picture. Transition on the slat can be clearly seen in the right infrared picture, indicated by the dark band between the dashed lines. Its location coincides with the kink in the pressure distribution after the pressure peak on the slat leading edge. Due to the low Reynolds number of the slat, transition will almost certainly be realised through a small laminar separation

205   bubble. It is followed by turbulent attached flow. Although the leading edge of the airfoil is not visible due to the presence of the slat, combining the pressure distribution and the infrared image shows that the main airfoil upper surface is laminar up to the mid-chord position, followed by an attached turbulent boundary layer.

Figure 6. Example of tuft visualisation obtained for a clean airfoil (i.e. no tripping) with a slat at $Re = 1.5 \cdot 10^6$ and a small angle of attack.
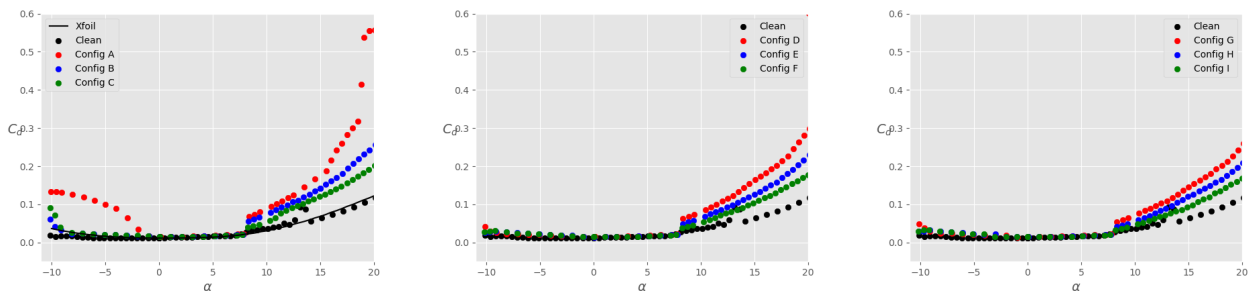
Figure 7. Total drag coefficient C_d on the ensemble airfoil+slat as a function of the angle of attack α, for different slat configurations, a clean main airfoil (i.e. no tripping), and $Re = 1.5 \cdot 10^6$: $h_{\text{slat}}/c_{main} = 0.02$ (left), $h_{\text{slat}}/c_{main} = 0.03$ (center), $h_{\text{slat}}/c_{main} = 0.04$ (right). The black data are taken without slat, while the coloured data is in the presence of a slat with $\beta_{\text{slat}} = 16.4°$ (red), $\beta_{\text{slat}} = 21.4°$ (blue), $\beta_{\text{slat}} = 26.4°$ (green). The results of Xfoil simulations for the clean main airfoil are shown by the continuous black line on the left plot.
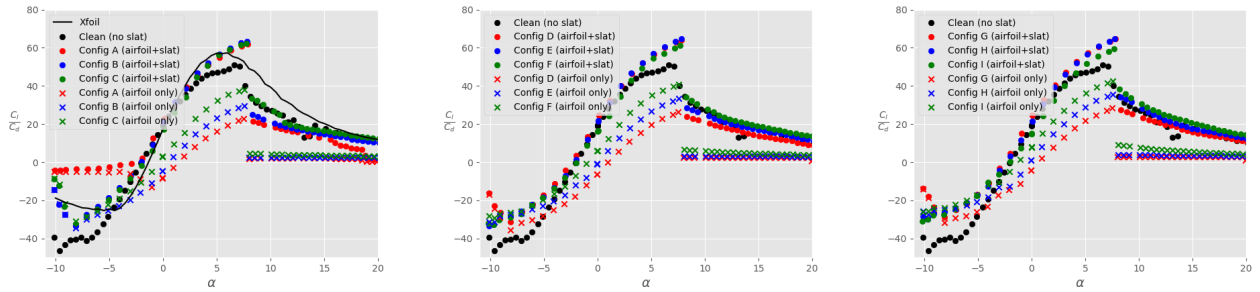
Figure 8. Lift-to-drag ratio C_l/C_d as a function of the angle of attack α for different slat configurations, a clean main airfoil (i.e. no tripping), and $Re = 1.5 \cdot 10^6$: $h_{\text{slat}}/c_{main} = 0.02$ (left), $h_{\text{slat}}/c_{main} = 0.03$ (center), $h_{\text{slat}}/c_{main} = 0.04$ (right). The black data are taken without slat, while the coloured data is in the presence of a slat with $\beta_{\text{slat}} = 16.4°$ (red), $\beta_{\text{slat}} = 21.4°$ (blue), $\beta_{\text{slat}} = 26.4°$ (green). Furthermore, dots represent the total lift coefficient (main airfoil + slat), whilst the crosses show the lift force on the main airfoil only. The results of Xfoil simulations for the clean main airfoil are shown by the continuous black line on the left plot.
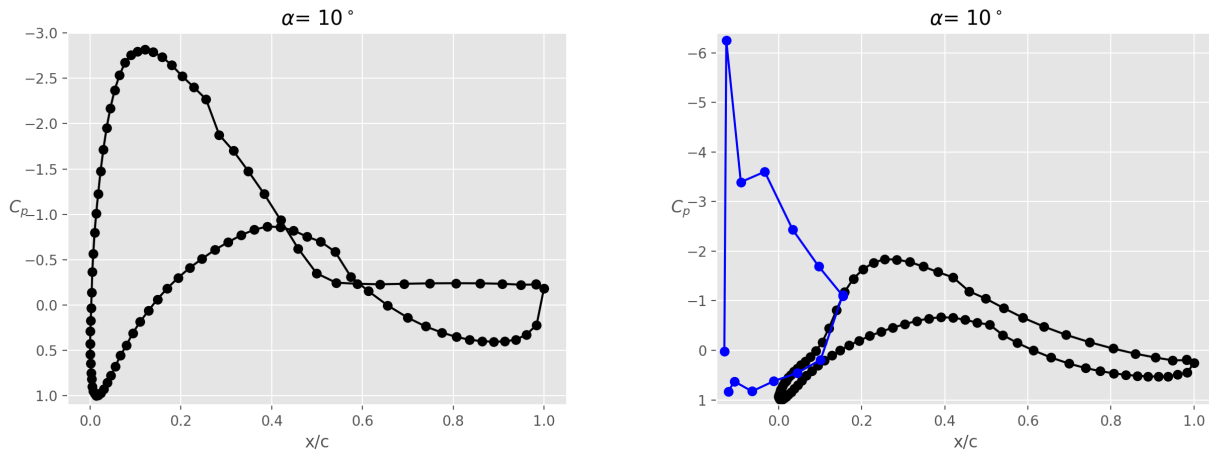
Figure 9. Pressure coefficient C_p at $\alpha = 10°$ for a clean main airfoil (i.e. no tripping): main airfoil alone (left), main airfoil with slat in case A (right), where both the pressure distributions on the main airfoil (black) and slat (blue) are shown.
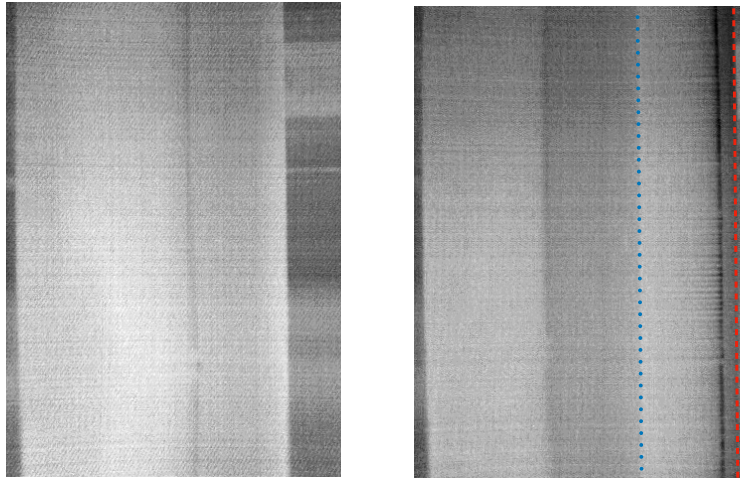
Figure 10. Infrared images of the suction side of the clean main airfoil (i.e. no tripping) at an angle of attack $\alpha = 10°$: without slat (left) and with slat under configuration A (right). In the right figure, the red dashed line indicates the slat leading edge, whilst the blue dotted line shows the slat trailing edge. Flow is going from right to left.

3.2 Sensitivity to roughness

In order to assess the sensitivity of the results to surface roughness, the boundary layer on the main airfoil is tripped using a zig-zag turbulator tape placed at the 10% chord location on both the pressure and suction sides. The tape height is calculated according to Braslow and Knox (1958) using a critical Reynolds number of 400. This leads to a tape of thickness $0.2mm$. Furthermore, the tape has a width of $6mm$ and an angle of $30°$. Figure 11 shows the lift coefficient C_l as a function of the angle of attack α for different slat configurations. The black dots again represent the lift coefficient in the absence of slat. As expected, but still highly undesirable, tripping the boundary layer significantly reduces the lift coefficient at low angles of attack. The negative effect of the zig-zag tape can be alleviated by using vortex generators, as shown in Fig. 12 for the main airfoil without slat. Note that the small abnormality in the lift coefficient at $\alpha \approx 13°$ for the clean case is not observed in the tripped case (with and without VGs). When the slat is mounted on the main airfoil, the zig-zag tape also leads to a loss of C_l at small angles of attack, although this effect is less pronounced than in the absence of slat (Figure 11). This observation is also made on the lift contribution coming from the main airfoil (not shown). At negative angles of attack, the lift coefficient on the ensemble airfoil+slat is almost identical to that of the airfoil without slat. Consequently, the presence of the slat decreases the contribution of the lift force coming from the main airfoil. This is not the case for positive angles of attack. In particular, for $\alpha > 5°$, the slat has no influence on the lift force experienced by the main airfoil only, as that contribution is identical to the lift force on the main airfoil without slat (not shown). This explains why the lift coefficient on the ensemble airfoil+slat is then larger than that of the airfoil without slat (Fig. 11). Additionally, similar trends than with the clean airfoil are obtained, namely an overall increase in C_l in the presence of a slat, with larger C_l as β_slat decreases. Also, there is a small decrease of C_l as h_slat increases, although this is very small.
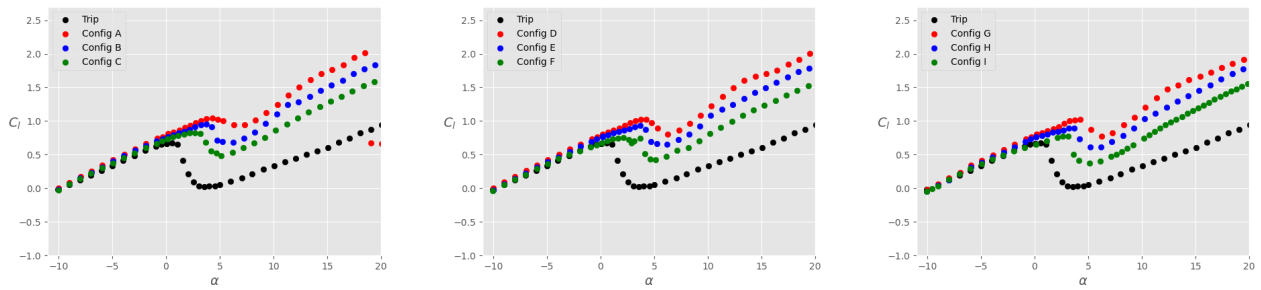
Figure 11. Total lift coefficient C_l on the ensemble airfoil+slat as a function of the angle of attack α, for different slat configurations, a tripped main airfoil, and $Re = 1.5 \cdot 10^6$: $h_{\text{slat}}/c_{main} = 0.02$ (left), $h_{\text{slat}}/c_{main} = 0.03$ (center), $h_{\text{slat}}/c_{main} = 0.04$ (right). The black data are taken without slat, while the coloured data is in the presence of a slat with $\beta_{\text{slat}} = 16.4°$ (red), $\beta_{\text{slat}} = 21.4°$ (blue), $\beta_{\text{slat}} = 26.4°$ (green).
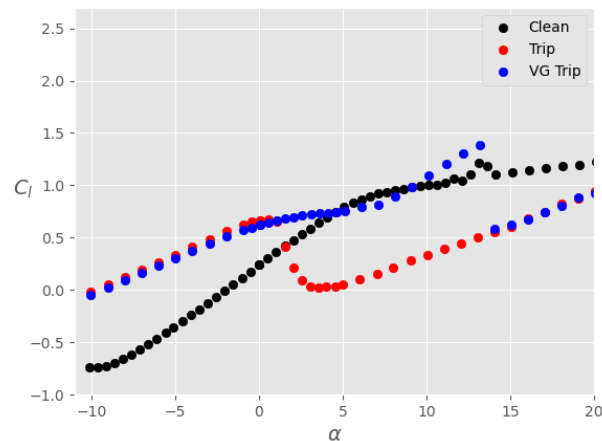
Figure 12. Lift coefficient C_l as a function of the angle of attack α for a main element without slat: clean airfoil without VGs (black), tripped airfoil without VGs (red), tripped airfoil with VGs (blue).

The drag coefficients are presented in Fig. 13. As expected, drag is larger in the tripped case compared to the clean results. However, the presence of the slat slightly decreases C_d at all positive angles of attack before stall. As for the results on the clean airfoil, the contribution of the slat to the total drag force is very small. The positive effect that the slat has on the overall drag reduction is therefore mostly due to the fact that the slat changes the flow field around the main airfoil. Figure 14 shows the lift-to-drag ratio for all the tripped configurations. As already mentioned before, the overall aerodynamic performance of the tripped system is smaller than in the clean case. The addition of a slat has a positive influence on the overall aerodynamic performance. However, as opposed to the clean cases, the ratio C_l/C_d computed on the airfoil alone (in the presence of a slat) is rather similar to that of the airfoil without slat (not shown here for the sake of graph clarity).
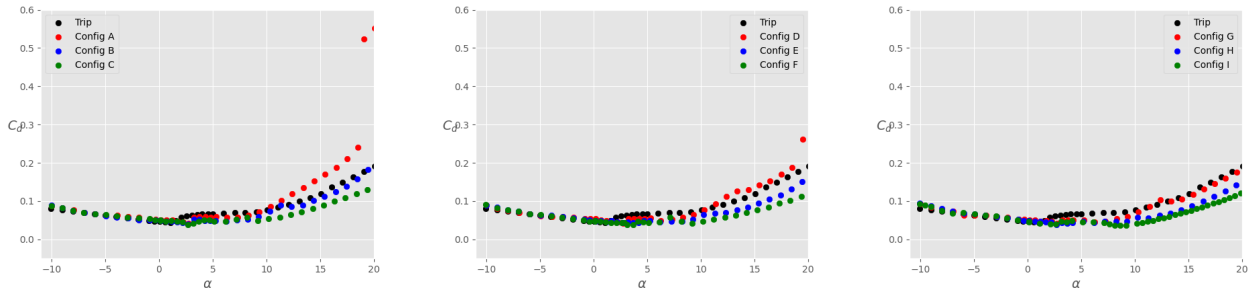
Figure 13. Total drag coefficient C_d on the ensemble airfoil+slat as a function of the angle of attack α for different slat configurations, a tripped main airfoil, and $Re = 1.5 \cdot 10^6$: $h_{\text{slat}}/c_{main} = 0.02$ (left), $h_{\text{slat}}/c_{main} = 0.03$ (center), $h_{\text{slat}}/c_{main} = 0.04$ (right). The black data are taken without slat, while the coloured data is in the presence of a slat with $\beta_{\text{slat}} = 16.4°$ (red), $\beta_{\text{slat}} = 21.4°$ (blue), $\beta_{\text{slat}} = 26.4°$ (green).
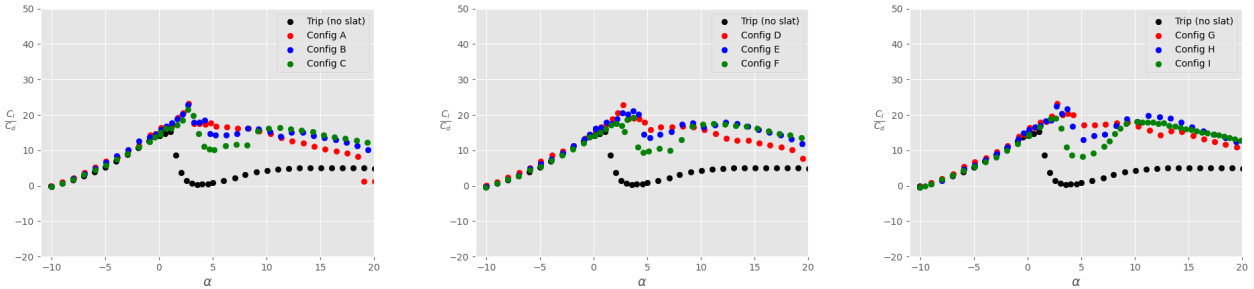
Figure 14. Lift-to-drag ratio C_l/C_d on the ensemble airfoil+slat as a function of the angle of attack α for different slat configurations, a tripped main airfoil, and $Re = 1.5 \cdot 10^6$: $h_{\text{slat}}/c_{main} = 0.02$ (left), $h_{\text{slat}}/c_{main} = 0.03$ (center), $h_{\text{slat}}/c_{main} = 0.04$ (right). The black data are taken without slat, while the coloured data is in the presence of a slat with $\beta_{\text{slat}} = 16.4°$ (red), $\beta_{\text{slat}} = 21.4°$ (blue), $\beta_{\text{slat}} = 26.4°$ (green).

Figure 15 shows infrared images of the flow ~~past~~ on the airfoil at $\alpha = 10°$, without (left) and with (right) slat. In the right figure, the red dashed line indicates the slat leading edge, whilst the blue dotted line shows the slat trailing edge. It can be seen that, in both cases, the flow is rather two-dimensional as expected. Also, the presence of the slat ~~leads to a more uniform flow~~ alleviates flow separation on the main airfoil. This is also apparent on the pressure coefficient shown in Fig. 16 for the same conditions.

3.3 Comparison of the performances with VGs

Figures 17 and 18 show the polars for the lift and drag coefficients, respectively, when the main airfoil is equipped with VGs instead of a slat (red dots). For comparison, results obtained with the slat under configuration A are also shown in these plots (blue dots). Again, both clean (left) and tripped (right) conditions are shown. In both conditions, it is clear that the lift coefficient is considerably increased due to the presence of the VGs, which suppress separation. The increase is however
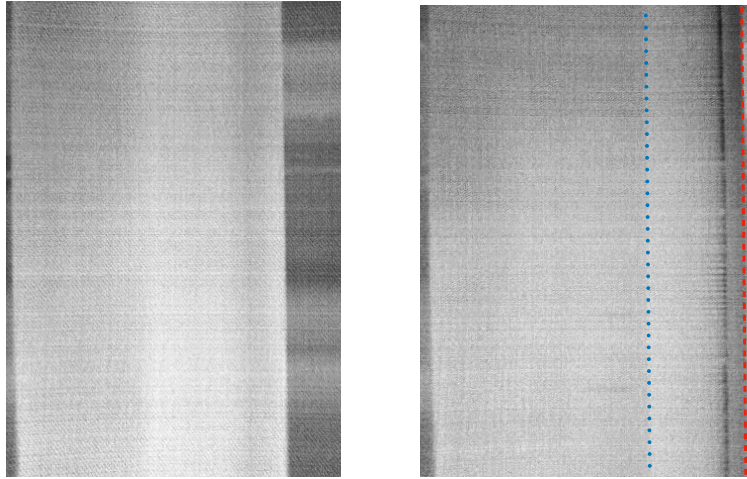
Figure 15. Infrared images of the suction side of the tripped main airfoil at an angle of attack $\alpha = 10°$: without slat (left) and with slat under configuration A (right). In the right figure, the red dashed line indicates the slat leading edge, whilst the blue dotted line shows the slat trailing edge.
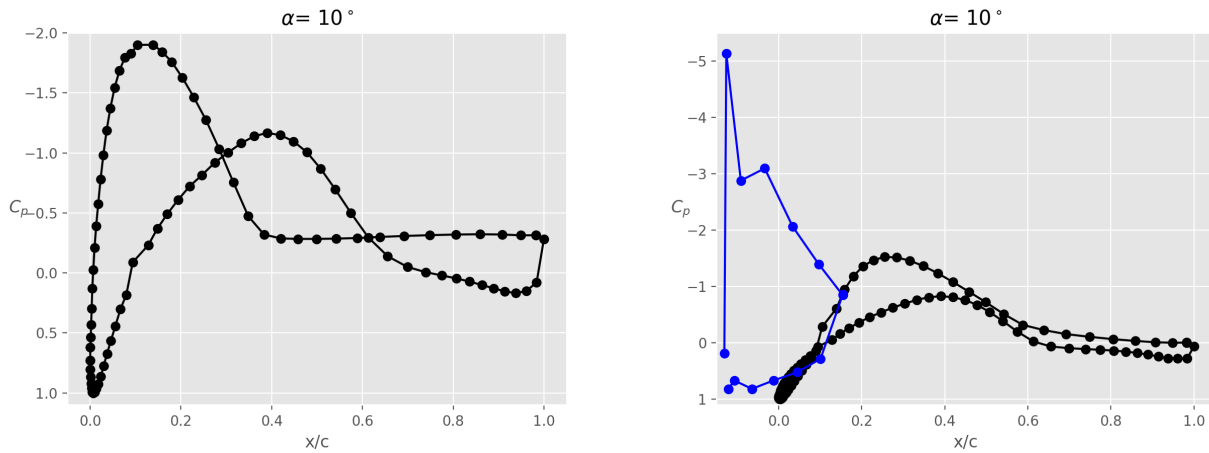
Figure 16. Pressure coefficient C_p at $\alpha = 10°$ for a tripped main airfoil: main airfoil alone (left), main airfoil with slat in case A (right), where both the pressure distributions on the main airfoil (black) and slat (blue) are shown.

245 smaller than when a slat is used. Furthermore, at small positive angles of attack, the lift-to-drag ratio is reduced in the presence of the VGs in the clean case (Fig. 19, left), which is not the case with a slat. The aerodynamic performances obtained with VGs are larger than with the slat only in the tripped conditions and for $6° < \alpha < 14°$, where the small gain in C_l brought by the slat is not enough to compensate for the small associated increase in C_d. Outside of this range of angles of attack, the slat seems to be aerodynamically more advantageous than VGs, at least for the conditions investigated here. Of course, the slat brings

250 additional challenges for the structural design of the blade, which are not taken into account in this study.
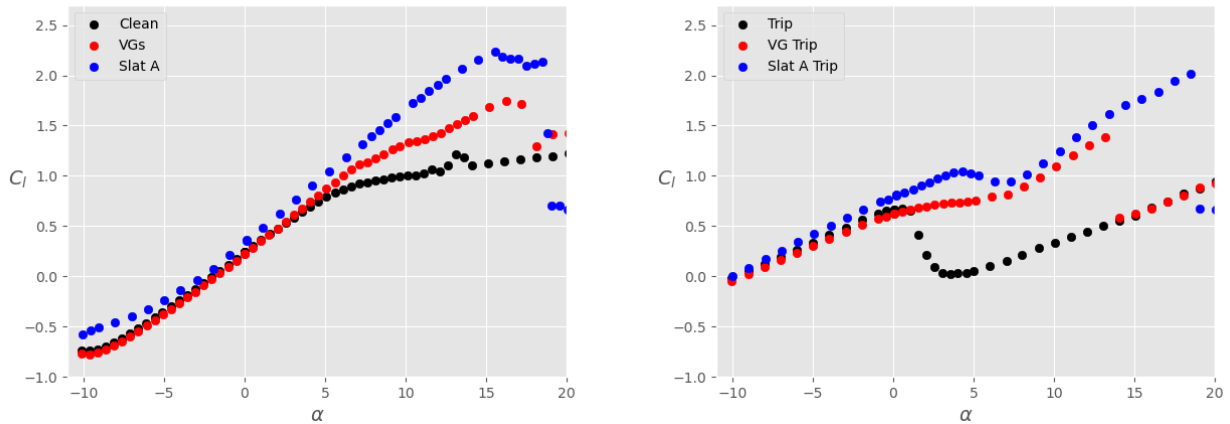
Figure 17. Lift coefficient C_l as a function of the angle of attack α for the main airfoil at $Re = 1.5 \cdot 10^6$, without VGs and without slat (black), with VGs only (red), and with slat only in configuration A (blue). Left: clean airfoil; right: tripped airfoil.
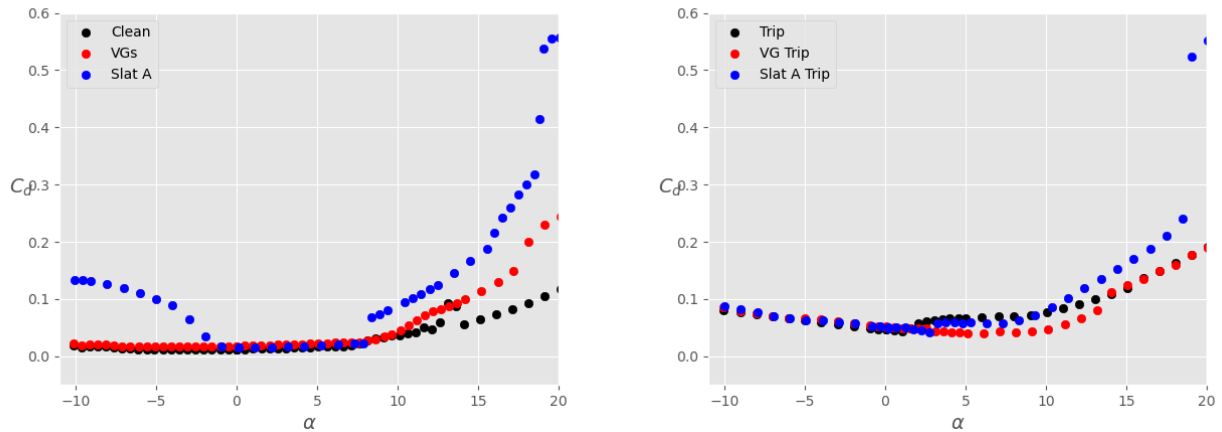
Figure 18. Drag coefficient C_d as a function of the angle of attack α for the main airfoil at $Re = 1.5 \cdot 10^6$, without VGs and without slat (black), with VGs only (red), and with slat only in configuration A (blue). Left: clean airfoil; right: tripped airfoil.
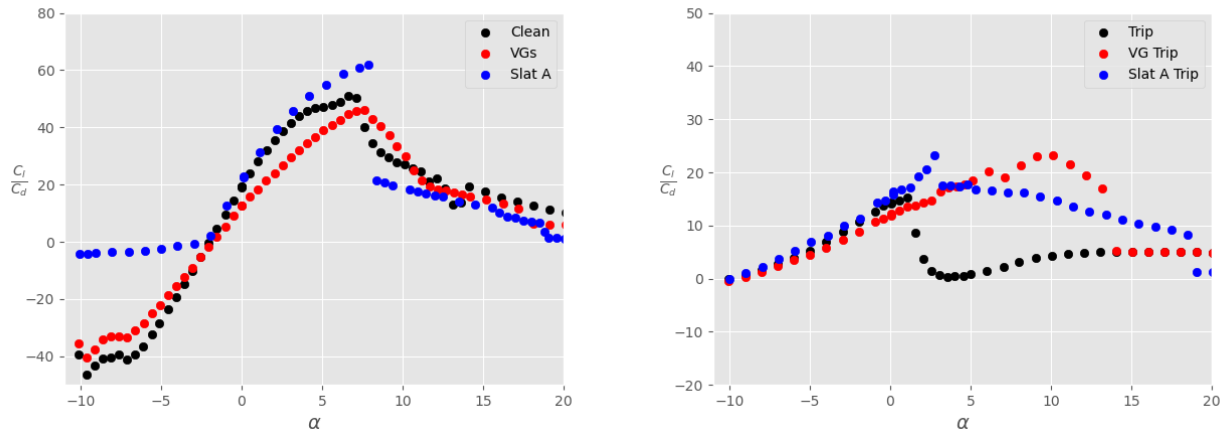
Figure 19. Lift-to-drag ratio C_l/C_d as a function of the angle of attack α for the main airfoil at $Re = 1.5 \cdot 10^6$, without VGs and without slat (black), with VGs only (red), and with slat only in configuration A (blue). Left: clean airfoil; right: tripped airfoil.

4   Conclusions

This paper summarises the main results obtained from wind tunnel experiments on a DU00-W2-401 airfoil, equipped with either a slat or vortex generators, in both clean and tripped conditions. The results suggest that the use of a slat can significantly increase the aerodynamic performance of the system. For a clean airfoil and small angles of attack, the presence of a slat decreases the lift-to-drag ratio of the main airfoil only. This is in line with the slat effect described in the literature (Smith, 1975). However, because of the positive lift on the slat itself, the overall lift-to-drag ratio of the ensemble airfoil+slat is either equal to, or larger than, that of the airfoil without slat. As the angle of attack increases beyond approximately $7°$ to $10°$, the presence of a slat modifies the flow field around the main airfoil in such a way that the aerodynamic performance of the latter alone is increased. The overall lift-to-drag ratio is therefore largely better than without using a slat. This is in line with the results from CFD simulations obtained in similar conditions (Steiner et al., 2020). The slat also clearly delays stall, as documented in the literature. The present results show some dependencies of the lift coefficient to the position and angular orientation of the slat. In particular, for the range of parameters investigated here, larger slat angles up to $\beta_{\text{slat}} = 26.4°$ usually lead to smaller values of C_l. Increasing the gap between the slat and the main airfoil up to $h_{\text{slat}}/c_{\text{main}} = 0.04$ can lead to slightly better values of C_l, which suggests . This confirms that there is an optimal gap between the slat and the airfoil, beyond which the performance will likely decrease again (AGARD-CP-515, 1993). When the airfoil is tripped, the presence of a slat is beneficial at all positive angles of attack and does not change the aerodynamic performances at negative angles of attack, compared to the case of an isolated airfoil. It is also shown that the use of a slat can partly alleviate the loss of lift at low angles of attack under tripped conditions.

~~The~~ Based on these results, the present study shows that using a slat on a wind turbine blade could be beneficial provided that the slat angle is not too large and the gap width not too small. It is however important to bear in mind that the present conclusions hold for the geometries and parameters investigated here and do not consider any structural challenges that arise when attaching a slat to a wind turbine blade. In particular, the effect of the slat on the overall blade mass and aeroelastic responses, as well as the logistics of attaching the slat to the blade, are aspects that would need further analysis. Future work should therefore focus on incorporating these aspects in the overall assessment of the feasibility and potential of using slats on commercial wind turbine blades.

Appendix A: Values of the angles of attack delimiting the use of either the wake-rake drag or the pressure drag

Table A1 lists, for each case presented in this paper, the angle of attack below which the wake rake drag is used for the calculation of C_d.

Table A1. Values of angles of attack below which the wake-rake drag is used.

Airfoil condition	VG present	Slat configuration	α [°]
Clean	No	None	8
Clean	Yes	None	14
Clean	No	A	15
Clean	No	B	21
Clean	No	C	23.5
Clean	No	D	19
Clean	No	E	21
Clean	No	F	21
Clean	No	G	19
Clean	No	H	23
Clean	No	I	25
Trip	No	None	1.5
Trip	Yes	None	3
Trip	No	A	3
Trip	No	B	3
Trip	No	C	3
Trip	No	D	3
Trip	No	E	3
Trip	No	F	3
Trip	No	G	3
Trip	No	H	3
Trip	No	I	3

Acknowledgements

280 The authors would like to acknowledge Rijksdienst voor Ondernemend Nederland (RVO) through the TSE Hernieuwbare Energie funding scheme (ABIBA project). We are also grateful for the technical support of Stefan Bernardy and Emiel Langendijk of the Low-speed Laboratory in helping with the design and preparation of the model setup. We also would like to thank Wind Tunnel Services. Finally Nicholas Balaresque of Deutsche WindGuard is acknowledged for giving us the opportunity to use their DU00-W2-401 airfoil model as basis for the measurements.

References

AGARD-AG-109: Subsonic wind tunnel wall corrections, Technical report RDP AGARD-AG-109, AGARD, 1966.

AGARD-AG-336: Wind tunnel wall corrections, Technical report RDP AGARD-AG-336, AGARD, 1998.

AGARD-CP-515: High-lift system aerodynamics, Technical report RDP AGARD-CP-515, AGARD, 1993.

Allen, H. and Vincenti, W.: Wall interference in a two-dimensional wind tunnel, with consideration of the effect of compressibility, Report 782, NACA, 1944.

Bach, A.: Gurney Flaps and Micro-Tabs for Load Control on Wind Turbines, Ph.D. thesis, Technische Universität Berlin, 2016.

Baldacchino, D.: Vortex Generators for Flow Separation Control Wind Turbine Applications, Ph.D. thesis, Delft University of Technology, 2019.

Braslow, A. and Knox, E.: Simplified method for determination of critical height of distributed roughness particles for boundary-layer transition at Mach numbers from 0 to 5,, Technical Note 4363, National Advisory Committee For Aeronautics, 1958.

LeBlanc, B., Viré, A., Steiner, J., Timmer, N., Langedijk, E., and Bernardy, S.: ABIBA Airfoil and Slat Measurement Data, 4TU.ResearchData. Dataset. https://doi.org/10.4121/14170442.v2, 2021.

Liebeck, R.: Design of subsonic airfoils for high lift, Journal of Aircraft, 15, 547–561, 1978.

Manso Jaume, A. and Wild, J.: New results in Numerical and Experimental Fluid Mechanics X, chap. Aerodynamic Design and Optimization of a High-Lift Device for a Wind Turbine Airfoil, Springer Internatinal Publishing, 2016.

Pechlivanoglou, G., Nayeri, C., and Paschereit, C.: Fixed leading edge auxiliary wing as a performance increasing device for HAWT blades, in: Proceedings of the DEWEK conference, 2010.

Schramm, M., Stoevesandt, B., and Peinke, J.: Simulation and Optimization of an Airfoil with Leading Edge Slat, J. Phys.: Conf. Ser., 753, 2016.

Schubauer, G. and Spangenberg, W.: Forced mixing in boundary layers, J. Fluid Mechanics, 8, 10–32, 1960.

Smith, O. A. M.: High-Lift Aerodynamics, Journal of Aircraft, 12, 501–530, 1975.

Steiner, J., Viré, A., Benetti, F., Timmer, N., and Dwight, R.: Parametric slat design study for thick base airfoils at high Reynolds numbers, Wind Energy Science, 2020.

Velte, C., Hansen, M., and Okulov, V.: Multiple vortex structures in the wake of a rectangular winglet in ground effect, Experimental Thermal and Fluid Sciences, 72, 31–39, 2016.

Wentz, W.: Effectiveness of Spoilers on the GA(W)-1 Airfoil With a High- Performance Fowler Flap, Technical report NASA-CR-2538, NASA, 1975.

Zahle, F., Guanaa, M., Sorensen, N., and Bak, C.: Design and Wind Tunnel Testing of a Thick, Multi-Element High-Lift Airfoil, in: European Wind Energy Conference and Exhibition, p. 11, 2012.

Author contribution

AV: original manuscript, post-processing and interpretation of results, funding acquisition, responsible supervisor. BL: scientist in charge of the experiment (preparation, run, post-processing), interpretation of results, manuscript revisions. JS: support with model design and parameters, interpretation of results, manuscript revisions. NT: support to prepare the experiment, interpretation of results, responsible of the wind tunnel facility.